Rare Metal Materials and Engineering
Volume 54, Issue 3, March 2025
Available online at www.rmme.ac.cn

Science Press

Cite this article as: Li Danni, Yao Zhengjun, Yao Mengxin, et al. Microstructure and Properties of Fe-Mo Functionally Graded Materials Fabricated by Electron Beam-Directional Energy Deposition[J]. Rare Metal Materials and Engineering, 2025, 54(03): 554-568. DOI: https://doi.org/10.12442/j.issn.1002-185X.20240549.

ARTICLE

Microstructure and Properties of Fe-Mo Functionally Graded Materials Fabricated by Electron Beam-Directional Energy Deposition

Li Danni[1,2], Yao Zhengjun[1,2], Yao Mengxin[1], Zhang Shuxian[1], Moliar Oleksandr[3], Soloviova Tetiana[3], Trosnikova Iryna[3], Loboda Petro[3], Zhang Shasha[1]

[1] College of Materials Science and Technology, Nanjing University of Aeronautics and Astronautics, Nanjing 211100, China; [2] Key Laboratory of Materials Preparation and Protection for Harsh Environment, Ministry of Industry and Information Technology, Nanjing 210016, China; [3] Igor Sikorsky Kyiv Polytechnic Institute, National Technical University of Ukraine, Kyiv 03056, Ukraine

Abstract: Fe-Mo functionally graded materials (FGMs) with different composition-change rates from 100% 304 stainless steel to 100% Mo along the composition gradient direction were prepared by electron beam-directed energy deposition (EB-DED) technique, including three samples with composition mutation of 100%, composition change rate of 10% and 30%. Results show that the composition-change rate significantly affects the microstructure and mechanical properties of the samples. In the sample with abrupt change of composition, the sharp shift in composition between 304 stainless steel and Mo leads to a great difference in the microstructure and hardness near the interface between the two materials. With the increase in the number of gradient layers, the composition changes continuously along the direction of deposition height, and the microstructure morphology shows a smooth transition from 304 stainless steel to Mo, which is gradually transformed from columnar crystal to dendritic crystal. Elements Fe, Mo, and other major elements transform linearly along the gradient direction, with sufficient interlayer diffusion between the deposited layers, leading to good metallurgical bonding. The smaller the change in composition gradient, the greater the microhardness value along the deposition direction. When the composition gradient is 10%, the gradient layer exhibits higher hardness (940 HV) and excellent resistance to surface abrasion, and the overall compressive properties of the samples are better, with the compressive fracture stress in the top region reaching 750.05±14 MPa.

Key words: functionally graded materials; EB-DED; microstructure evolution; mechanical properties

1 Introduction

The rapid development of aerospace, nuclear power, ships, and other engineering fields demands increasingly high performance from components operating in extreme conditions[1–2]. The perforated head, a crucial part of seamless steel tube production, is exposed to temperature surpassing 1000 °C, complex stresses, and surface friction, creating challenging service conditions[3–4]. To prolong the service life, the perforated head must satisfy the demands of high temperature, high stress, and high friction. Low-alloy steel, traditionally used as a material for perforated heads, is prone to problems such as nose collapse, steel sticking, and cracking. These issues significantly impact the service life of perforated heads and the dimensional accuracy of seamless steel pipes[5]. Pure molybdenum, known for its high melting point, strength, wear resistance, and thermal conductivity, has become the primary material for preparing perforated heads, gradually replacing low-alloy steel. However, pure molybdenum is expensive, lacks plasticity and toughness, and is prone to cracking after prolonged perforation at high temperature, which greatly restricts its potential applications[6].

Currently, a new type of piercing plug has been developed[7]. It uses die steel as the plug matrix, with a

Received date: August 23, 2024
Foundation item: National Natural Science Foundation of China (51975286)
Corresponding author: Yao Zhengjun, Ph.D., Professor, College of Materials Science and Technology, Nanjing University of Aeronautics and Astronautics, Nanjing 211100, P. R. China, E-mail: yaozj1921@126.com

molybdenum nose embedded into the plug and a hardened alloy layer of Fe-Mo bimetal formed by metallurgical bonding. This unique preparation of Fe and Mo as a bimetallic material structure allows for the benefits of both alloys to be realized while reducing material costs. 304 stainless steel is an ideal choice for mold manufacturing due to its resistance to corrosion and heat[8]. However, the thermal expansion coefficients of 304 stainless steel is different from molybdenum and its alloys, and when directly connected, intermetallic compounds may form at the interface, leading to stress concentration and cracking[9]. Functionally graded material (FGM) is a new type of composite material that combines two or more materials by changing the composition of the materials through a gradient[10–11]. This gradient change in the microstructure and properties of the parts results in better mechanical properties in the gradient region. By preparing Fe-Mo FGMs, the composition transition between two metals can greatly reduce stress concentration and cracking[12].

The traditional methods of preparing FGMs include vapor deposition[13], centrifugal casting[14], powder metallurgy[15], etc. However, these methods have various drawbacks such as difficulty in regulating continuous gradient changes, poor interfacial bonding performance, and low long-term stability. These issues restrict the ability to fully utilize the performance advantages of FGMs. Additive manufacturing (AM) technique uses high-energy beams, such as laser, arc, or electron beams, as a heat source. By using high-energy beam currents to melt powder or wire and depositing material layer-by-layer, near-net shaping and good metallurgical bonding between layers can be achieved[10]. AM provides a new way to prepare FGMs by depositing materials layer-by-layer, enabling precise control of composition and multiple structures at the microscopic level[16]. Osipovich et al[17] used a double-feeder electron beam AM method to adjust the copper/steel gradient content in the transition zone by adjusting the feed rate, forming a steel-copper FGM with a gradient structure, complete interlayer deposition in the sedimentary body, and no defects such as cracks. And it was determined that the solidification of copper mainly occurred in the inter-dendritic gap along the direction of the main axis of the steel dendrites. Shu et al[18] successfully obtained a gradient plating by depositing T2 copper violet on AISI-304 stainless steel using electron beam free-forming technique. The microstructure of the deposited layers and the interface between neighboring layers were studied, and the results showed that the distribution of element Fe was more uniform with the increase in the number of Cu plating layers. Chen et al[19] prepared TC4(Ti6Al4V)-316L stainless steel FGM using the wire arc AM process. During the preparation, they carried out the wire feeding process along with tungsten inert gas shielded welding, adjusted the wire feeding speed (WFS) and deposited different mass percentages of Fe for each layer along the sample stacking direction, pointing out the advantages of good corrosion resistance, high specific strength, and low cost of TC4(Ti6Al4V)-316L FGM. Zuback et al[20] used the laser-directed energy deposition technique to obtain functionally gradient transition joints between ferrite and austenite alloys using compositional gradient joints instead of heterogeneous joints, reducing carbon loss from ferrite alloys due to sudden changes in the carbon chemical potential and demonstrating the effectiveness of gradient joints under service conditions. Shah et al[21] investigated the effects of laser power and powder feed rate on microstructure and properties, discovering that controlling carbide generation through input parameters allows for the selective preparation of materials with specific hardness and wear resistance. In summary, these studies mainly focus on the two aspects of forming process regulation and performance optimization. There are few studies on the effect of compositional change rate on the interfacial bonding properties and microscopic defects of FGMs[10].

Electron beam-directed energy deposition (EB-DED) technique, as a kind of AM technique, utilizes the electron beam flow as the heat source, and feeds the same or different types filaments into the molten pool simultaneously or alternately by changing the WFS in a high vacuum environment, to realize the flexible regulation of the composition ratio of each deposition layer[22].

In this study, Fe-Mo FGMs with different compositional change rates were prepared using EB-DED technique. Regulate the WFS of 304 stainless steel and Mo wire to explore the changing rules of microstructure, elemental changes, microhardness, friction and wear, and compression properties. Through experiments and data analysis, the new design principles to improve the interfacial bonding properties and overall mechanical properties of FGMs were proposed. These principles also guide the application of high-performance parts in various environments.

2 Experiment

For the experiments, 304 stainless steel wire and Mo wire with the diameter of 1.2 mm were used as raw materials. The 304 stainless steel with dimensions of 150 mm×100 mm×10 mm was used for the substrate. The chemical composition of the Mo wire and the substrate is given in Table 1 and Table 2, respectively.

Fig. 1 shows the schematic diagram of the EB-DED equipment system, which mainly consists of an electron gun, vacuum system, wire feeder, work platform and central control system. The deposition experiment was conducted in a vacuum environment with a pressure of 5×10^{-3} Pa. During

Table 1 Chemical composition of Mo wire (wt%)

Fe	Zr	La	Si	Ni	Mo
0.009	0.030	0.300	0.020	＜0.002	Bal.

Table 2 Chemical composition of 304 stainless steel substrate (wt%)

Cr	Ni	Mn	Si	C	Fe
19.300	9.050	1.780	0.470	0.020	Bal.

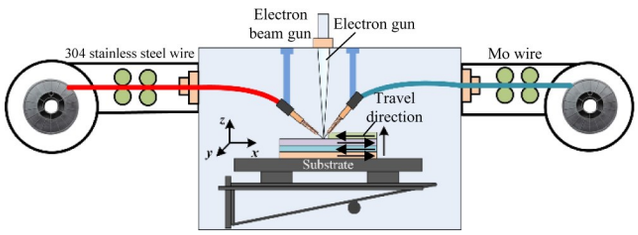

Fig.1 Schematic diagram of EB-DED process

fabrication, the electron gun emitted an electron beam, and the high-energy electron beam was irradiated onto the metal surface to form a molten pool. The metal wire was fed into the molten pool through the wire feed system and melted into a liquid in the molten pool. Layer-by-layer deposition was achieved by moving the working platform. The detail deposition parameters of EB-DED are given in Table 3. Due to the undercooling of the substrate during the initial deposition, in order to ensure the smooth forming, the substrate was firstly preheated 2–3 times. In addition, cooling should be carried out for 30 min during the continuous deposition process to prevent excessive heat accumulation from causing equipment damage or deposit collapse.

To investigate the effect of gradient compositional design on the deposited samples, three different thin-walled samples were prepared on 304 substrates using EB-DED technique. S1 refers to Fe-Mo bimetallic materials with abrupt compositional changes. S2 and S3 refer to Fe-Mo FGMs with a composition change rate of 10% and 30%, respectively. Fig. 2 shows schematic diagrams of the three thin-walled samples. By controlling the WFS of the two wires, each layer of S1, S2, and S3 samples with different composition design can be obtained. Table 4 lists the WFS corresponding to the composition of each layer. To maintain the same volume of material deposited per unit time, the WFS of the two materials was kept constant at any moment, with the sum of the WFS being 600 mm/min. The two wire materials were fed simultaneously at different WFSs to achieve the desired composition for each layer. The design compositions with respect to the WFS of 304 stainless steel (v_1) and Mo (v_2) are as Eq. (1)[23]:

$$\varphi_{304}(\text{wt}\%) = \frac{\rho_1 v_1}{\rho_1 v_1 + \rho_2 v_2} \quad (1)$$

where, v_1+v_2=600 mm/min, ρ_1 and ρ_2 are the densities of the 304 stainless steel and Mo, respectively, ρ_1=7.93 g/cm^3, and ρ_2 =10.23 g/cm^3.

Table 3 Basic parameters of EB-DED

Parameter	Value
Focusing current, I_f/mA	550
Beam current, I_b/mA	45
Travel speed, v_t/mm·min^{-1}	200
Total WFS, v_f/mm·min^{-1}	600

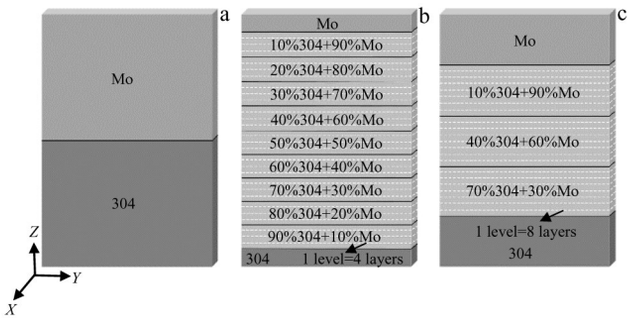

Fig.2 Composition design of three samples: (a) S1; (b) S2; (c) S3

Table 4 WFS corresponding to designed composition

Ratio of 304 stainless steel/wt%	Number of deposition layers	WFS of 304 stainless steel, v_1/mm·min^{-1}	WFS of Mo, v_2/ mm·min^{-1}
100	4	600	0
90	8	550	50
80	12	500	100
70	16	450	150
60	20	400	200
50	24	340	260
40	28	280	320
30	32	210	390
20	36	150	450
10	40	80	520
0	44	0	600

The microstructure and interface characteristics of the three thin-walled components were observed by Zeiss optical microscope (OM, Axio Imager. A2m) and scanning electron microscope (SEM, Hitachi S-4800). Fig. 3a is the schematic

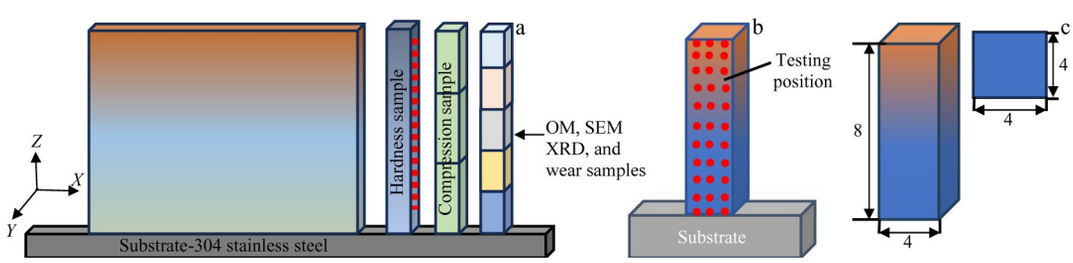

Fig.3 Schematic diagram of EB-DED thin-wall components: (a) OM, SEM, XRD and wear samples; (b) hardness testing position; (c) size of compression sample

diagram of the sampling location of the studied samples. The metallographic samples were polished with sandpaper and then polished using 50 nm SiO_2 polishing solution. And the samples were corroded using corrosion solutions of $FeCl_3$:HCl:H_2O=1:3:4 and $K_3[Fe(CN)_6]$:NaOH=1:1. The phase composition of the deposited samples and the diffusion distribution of chemical elements were analyzed by X-ray diffraction (XRD, Bruker D8-Advance) and energy dispersive X-ray spectroscope (EDS, X-flash Detector 5030).

The Vickers microhardness tester (HX-1000TM) was employed to measure the microhardness of different gradient interface regions, as shown in Fig. 3b. The applied load of 500 g and dwelling time of 10 s were set up. The compression tests (Zwick/Roll Z030TH) were conducted along the longitudinal direction of the metal deposition. The size of the compression sample is shown in Fig. 3c. The surface morphology and fracture morphology of the compressed samples were observed by SEM after loading to fracture at a compression loading rate of 0.2 mm/min. Linear reciprocating wear test (R-TEC MFT-5000) was conducted using a GCr15 steel ball with a diameter of 6.35 mm. Conducting tests were performed with a 4 mm stroke at a load of 12 N and a reciprocating speed of 4 mm/s for 10 min. After the friction wear test, the wear surface was observed with SEM. The three-dimensional (3D) profilometer (S neox) was used to test the 3D morphology of the wear scar. The cross section and volume wear of the wear scar were measured by the matching graphics processing software, and the specific wear rate was calculated by Eq.(2)[24]:

$$W = \frac{V}{PS} \tag{2}$$

where W is the specific wear rate ($m^3 \cdot N^{-1} \cdot m^{-1}$), V is the wear amount (m^3), P is the load (N), and S is the friction stroke (m).

3 Results

3.1 Microstructure analysis

Fig. 4 shows optical micrographs of the S1 sample in different compositional regions. It can be observed that unmelted Mo metal droplets (Fig. 4a) and a large number of cracks (Fig. 4b – 4f) appear at the interface of Mo and 304 stainless steel. The sample experienced a serious fracture, indicating that the S1 sample failed to achieve effective metallurgical bonding between Fe-Mo bimetals. The observed phenomenon was attributed to the significant difference in the coefficient of thermal expansion between Mo and 304 stainless steel. S1 sample was directly connected to the elemental composition interface of the sudden transition, resulting in stress concentration and the formation of brittle intermetallic compounds. During the electron-beam fused-wire deposition process, the mismatch in expansion and contraction led to elemental segregation, and the formation of cracks and microdefects. Additionally, the presence of many unmelted metal droplets in the deposition layer contributed to material fracture and failure[25–26].

The microstructures of S2 and S3 samples were observed using OM. Fig. 5 – Fig. 6 display the morphologies of the deposited samples from the bottom 304 stainless steel region to the top Mo. At the bottom, coarse columnar crystals are observed, gradually forming a preferred crystal orientation along the stacking direction and growing perpendicular to the substrate. Along the composition gradient, the microstructure boundary between adjacent deposited layers becomes gradually blurred, transforming into equiaxed crystals and then into fine dendritic crystals in the top region. There is good metallurgical bonding between various deposited transition layers. Microstructure changes in the S3 sample appear to be more significant than that in the S2 sample,

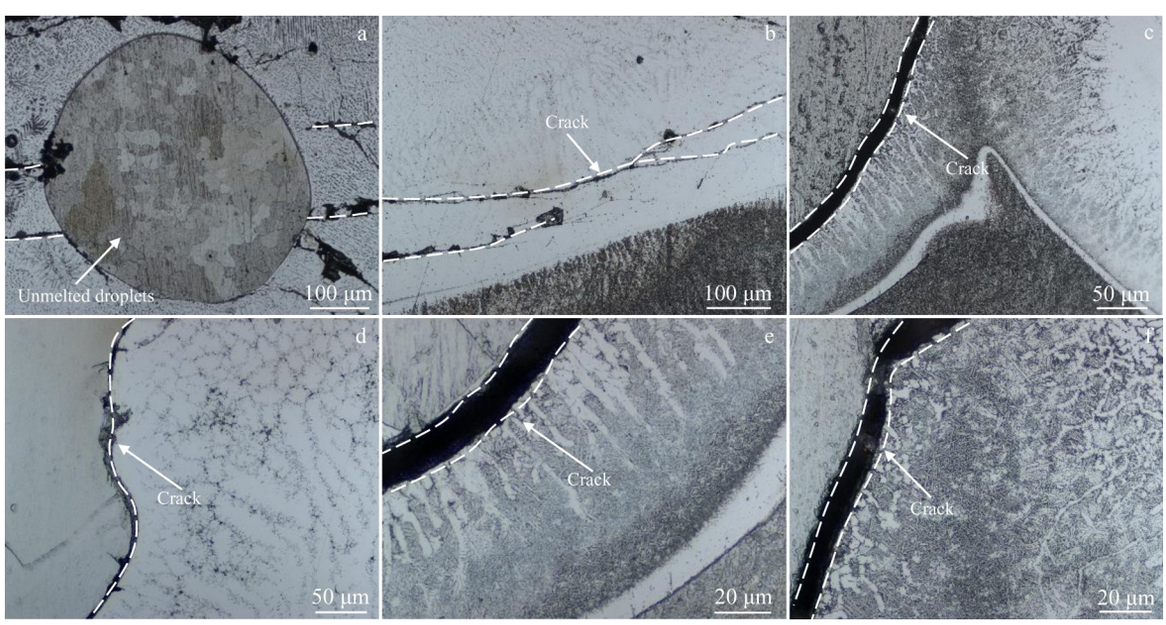

Fig.4 OM morphologies of S1 sample in different regions: (a) unmelted Mo droplets; (b–f) microcracks

particularly with the increase in the composition change rate.

The microstructures of the bottom region of the samples are depicted in Fig. 5a and Fig. 6a. It consists of columnar dendrites of γ-austenite and a small amount of residual δ-ferrite, with the columnar austenite growing along the direction of deposition (z-direction) and the δ-ferrite distributed at the γ-grain boundaries[27]. The microstructures of the intermediate region of the deposited thin wall are shown in Fig. 5b–5c and Fig. 6b – 6c. The morphologies of the S2 sample comprise homogeneous columnar crystals and cellular crystals, while the grains of the S3 sample show different morphologies with obviously biased aggregation. The sample is deposited layer-by-layer in a vacuum environment, and repeated thermal cycling increases the heat accumulation in the molten pool. The heat flow is dissipated through the 304 stainless steel substrate, and the cooling rate is relatively fast[28]. Under these conditions, the temperature gradient at the edge of the molten pool is the largest, and the solidification rate is relatively low, favoring the growth of cellular dendrites and resulting in longer columnar crystals and coarser cellular dendrites in the intermediate region.

In Fig. 5d and Fig. 6d, the microstructures of the top region of the formed samples, whose growth direction has been shifted, are mainly composed of dendrites. When the solidification proceeds to the top of the formed part, the temperature gradient direction of the solid/liquid interface changes from the deposition direction to the scanning speed direction. In creating the next layer by electron beam fuse deposition, the cladding layer will have a certain penetration depth, and the steering dendrite layer of the previous layer will be remelted. Therefore, only the top region of the whole formed sample retains the transformation of the dendrite growth direction during the complete solidification process[29–30].

Comprehensively comparing the microstructures of S1, S2, and S3 samples, it is found that there are obvious defects between the interfaces of S1 samples. And good metallurgical

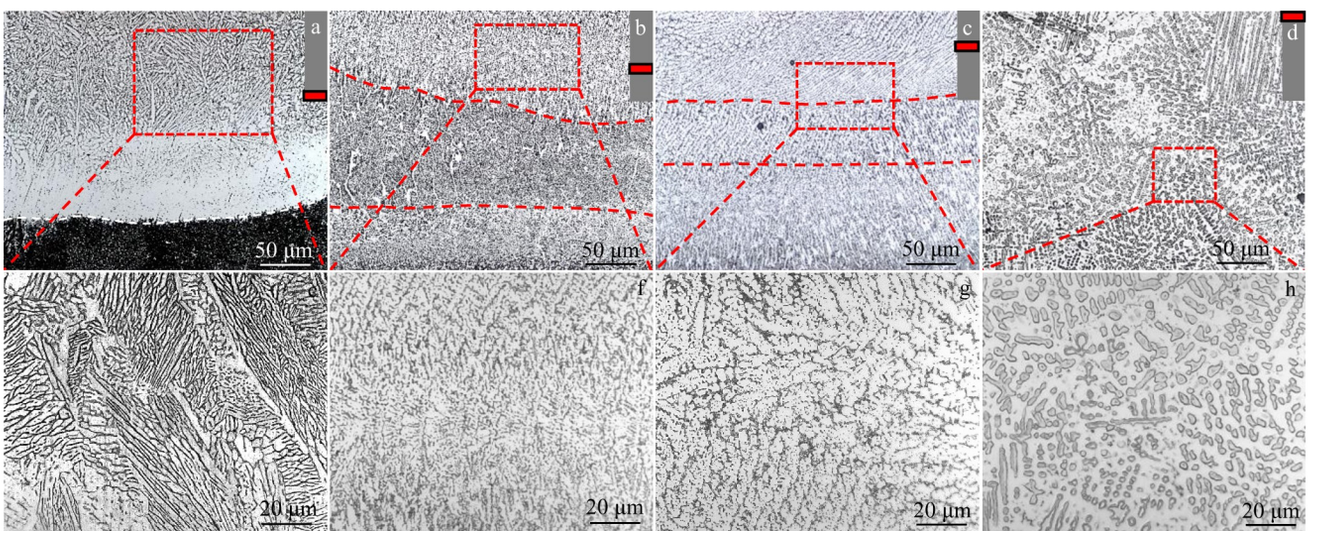

Fig.5 OM morphologies of S2 samples from bottom 304 stainless steel region to top Mo region: (a, e) bottom; (b–c, f–g) middle; (d, h) top

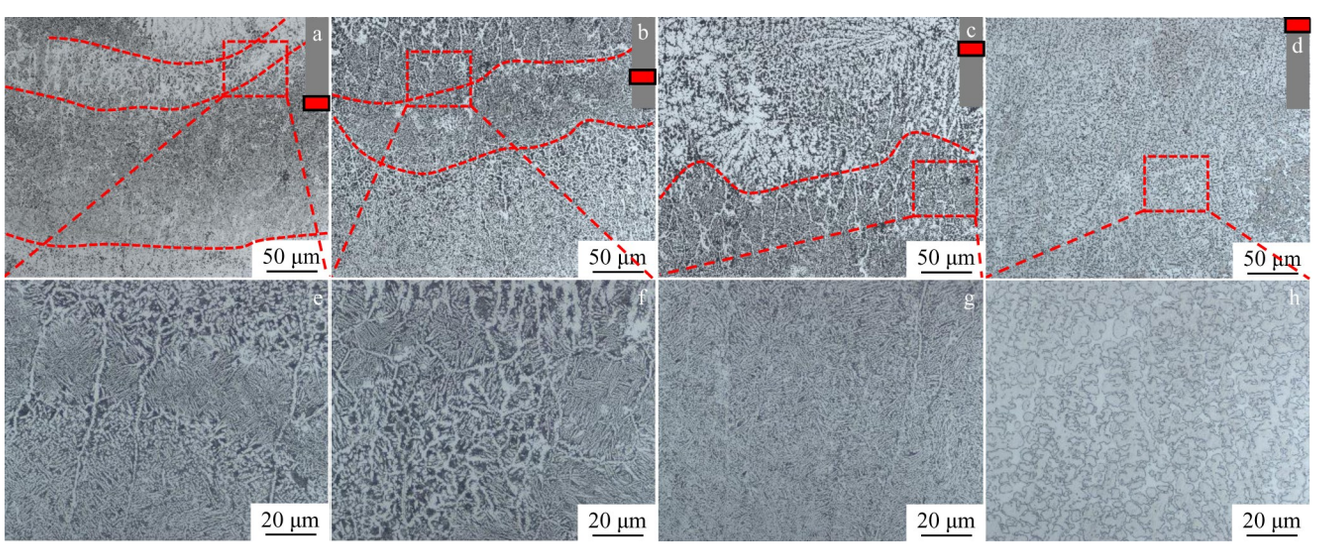

Fig.6 OM morphologies of S3 samples from bottom 304 stainless steel region to top Mo region: (a, e) bottom; (b–c, f–g) middle; (d, h) top

bonding between the interfaces of adjacent deposition layers fails to be formed. Whereas S2 and S3 samples, along the direction of the deposition height, form different microstructures, with continuous and uniform changes in the gradient transition layers and no defects, such as cracks, pores and other defects, and strong metallurgical bonding between the interfaces of adjacent layers is formed.

The microstructural transformation and elemental distribution of the top, middle, and bottom regions of S2 and S3 samples were analyzed by SEM and EDS. In Fig. 7–Fig. 8, the EDS element maps display the distribution of elements Mo and Fe at different regions. The changes in the distribution of these elements across the cross-section can be observed from the bottom region of 304 stainless steel to the top region containing Mo. Clear interfaces are visible in the different gradient transition regions, and there are noticeable differences in light and dark shades. The element Fe gradually decreases along the deposition direction (*z*-direction), whereas the element Mo gradually increases along the same direction. This pattern aligns with the intended composition change trend.

Comparing the trend of elemental distribution in Fig. 7 and Fig. 8, it is found that the distribution of elements Fe and Mo in S1 and S2 samples is almost the same. The distribution of elements along the deposition direction gradually transitions from Fe to Mo, and the change of elemental distribution at the interface is more obvious. Due to the stirring effect of the electron beam energy on the molten pool, good diffusion of elements Fe and Mo is realized, which alleviates the inhomogeneous phenomenon of stepwise elemental changes and lays the foundation for the metallurgical bonding of the subsequently deposited layers.

Fig. 9 and Fig. 10 demonstrate the SEM images and corresponding EDS line scanning results of the S2 and S3 sample interfaces, respectively. In the bottom region of the deposited sample, the difference in microstructure at the interface between 100% 304 stainless steel and 90% 304 stainless steel+10% Mo is obvious, and the interface is clear. With the increase in Mo content and the number of deposited layers, the mixed region exhibits a relatively homogeneous transition structure, and the layer interface of the sample gradually becomes blurred, as shown in Fig. 9i–9j. The EDS line scanning results confirm the fluctuation of the content of major alloying elements (Mo, Fe, Cr, and Ni) in the adjacent interfacial region. The content of element Mo gradually increases along the direction of sample deposition, while the content of elements Fe, Cr, Ni slowly decreases. S2 sample shows a smoother elemental change due to the small change rate of the composition, and the major elements Fe, Mo, Cr, and Ni in the gradient transition region along the direction of

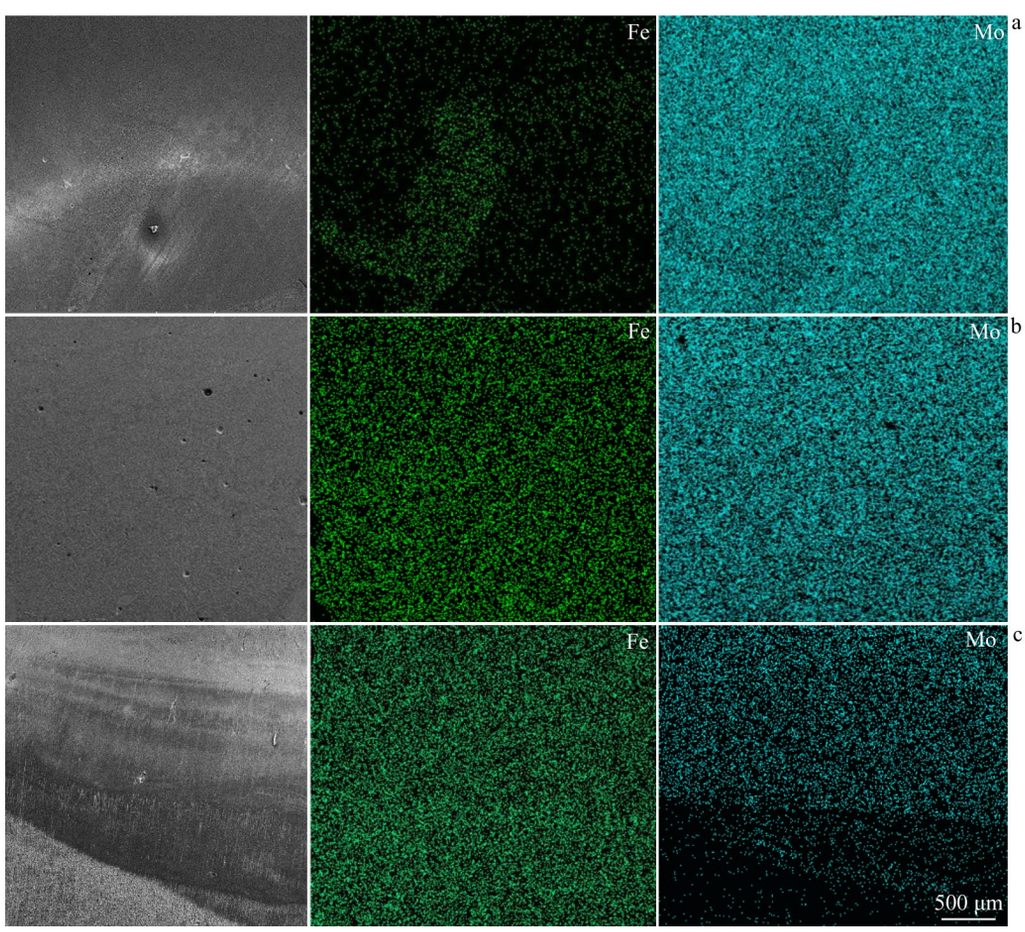

Fig.7 SEM images and corresponding element distribution in top (a), middle (b), and bottom (c) regions of S2 sample

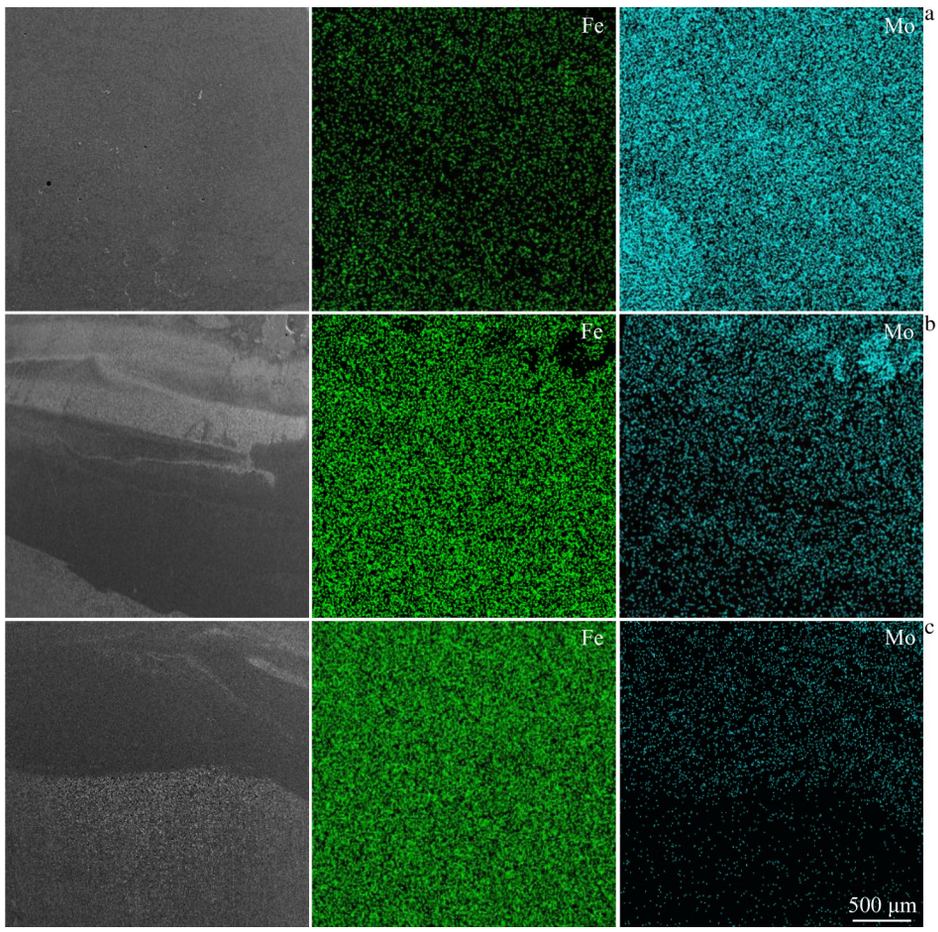

Fig.8 SEM images and corresponding element distribution in top (a), middle (b), and bottom (c) regions of S3 sample

the composition gradient show a good linear relationship. In each composition transition region, due to the impermissible dilution effect, the content of each element gradually changes, alleviating the uneven phenomenon of stepwise elemental changes, which is the result of full diffusion between layers. For the S3 sample with a compositional change rate of 30%, the elemental content of Fe, Mo, Cr, and Ni shows a certain degree of nonlinear relationship. The elemental content at the interface changes sharply, and the elemental transition is not smooth. A comprehensive analysis of the above shows that the reduction of the composition gradient will promote the uniform transition of the composition without elemental abnormal distribution and sharp changes, eliminating the sudden microstructure change in the layer interfacial connection of the heterogeneous materials, which makes the microstructure transition uniform, and ensures the overall performance of the functional gradient material at the same time.

3.2 Phase composition in gradient direction

The XRD patterns of the different gradient-deposited layers of S2 and S3 samples can be found in Fig.11 and Fig.12. The main phase in the 304 matrix is face-centered cubic (fcc) austenite. With an increase in Mo content and the number of deposited layers, new peaks not corresponding to the γ-phase or the pure Mo phase in 304 stainless steel appear in the S2 and S3 samples, indicating the presence of a secondary phase. The S2 sample forms the Fe_2Mo_3 strengthened phase in the deposited layers of 80% 304 stainless steel+20% Mo, while the S3 sample similarly forms the Fe_2Mo_3 strengthened phase in the deposited layers of 70% 304 stainless steel+30% Mo. This suggests that the S2 and S3 samples have the same phase composition when the rate of compositional change is different. The XRD results are analyzed to conclude that the phase transformation process of S2 and S3 thin-walled samples is $Fe_3Mo \rightarrow Fe_2Mo_3 \rightarrow Fe_{63}Mo_{37} \rightarrow Fe_7Mo_3$. Along the deposition direction of the samples, the intensity of the Fe_2Mo_3 diffraction peaks is gradually increases, while the intensity of the Fe_3Mo diffraction peaks is gradually weakened.

3.3 Effect of composition change rate on microhardness

Microhardness testing reflects the strength and wear resistance of a material. As can be seen in Fig. 13, the microhardness values of single 304 stainless steel at the bottom of the deposited layer are approximately 200 HV, with minimal changes. The microhardness curve of S1 sample shows a sharp increase near the fusion line and irregular fluctuations overall. As for the S2 sample with a compositional change rate of 10%, the curve demonstrates a continuous increase in microhardness along the deposition direction near the gradient deposition layer, reaching a maximum microhardness value of 940 HV. In contrast, the

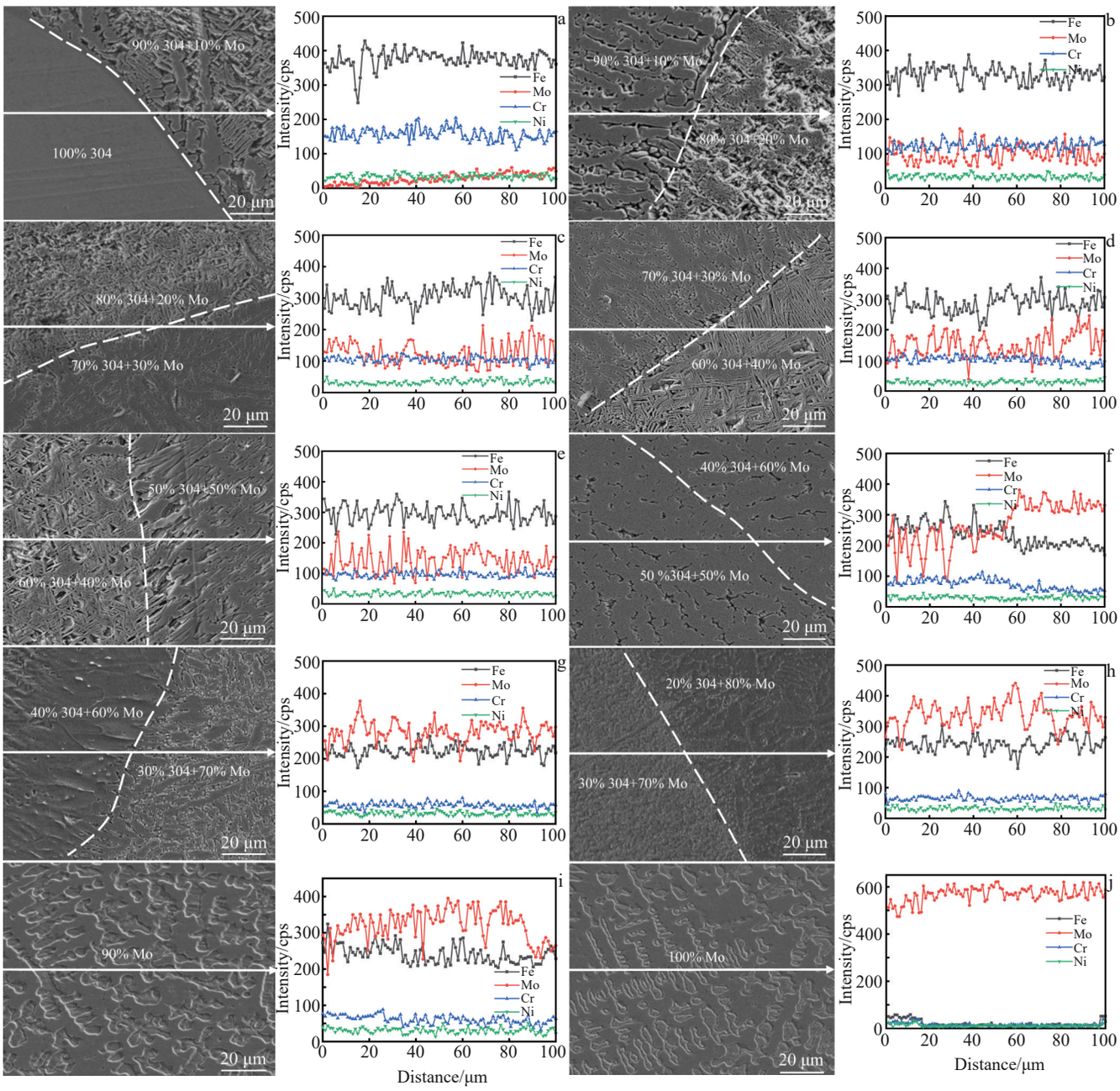

Fig. 9 SEM images and EDS line scanning results of adjacent interfaces with different Mo content on *y-z* plane of S2 sample: (a) 0%–10%; (b) 10%–20%; (c) 20%–30%; (d) 30%–40%; (e) 40%–50%; (f) 50%–60%; (g) 60%–70%; (h) 70%–80%; (i) 90%; (j) 100%

microhardness curve of the S3 sample with a compositional change rate of 30% reveals a higher maximum microhardness value but an overall lower value.

Combined with the above analysis, the direct connection of the S1 sample will form brittle intermetallic compounds, which are harmful to the interface, resulting in uneven microhardness distribution and irregular changes in the curve[26]. For Fe-Mo FGMs, the composition gradient change can reduce the heat accumulation between the Fe-Mo interface to reduce the thermal stress effect on the interfacial properties. According to the analysis of the microstructure evolution results, the gradient layer shows a fine and uniform grain structure in the sample with a composition change rate of 10%. From the Hall-Petch formula[31], the finer the grain size, the better the strengthening effect and the higher the microhardness value, which is consistent with the microhardness curve of the S2 sample.

3.4 Tribological behavior

Fig. 14 shows the friction and wear curves of the S2 and S3 samples and their corresponding average coefficients of friction (COF). The results show that the COF of the samples are in the range of 0.50–0.75 at a load of 12 N. The COF is one of the most important indexes characterizing the friction and wear performance, which is independent of the contact area and the sliding speed, and mainly reflects the surface roughness of the sample[32]. It can be observed from Fig. 14a

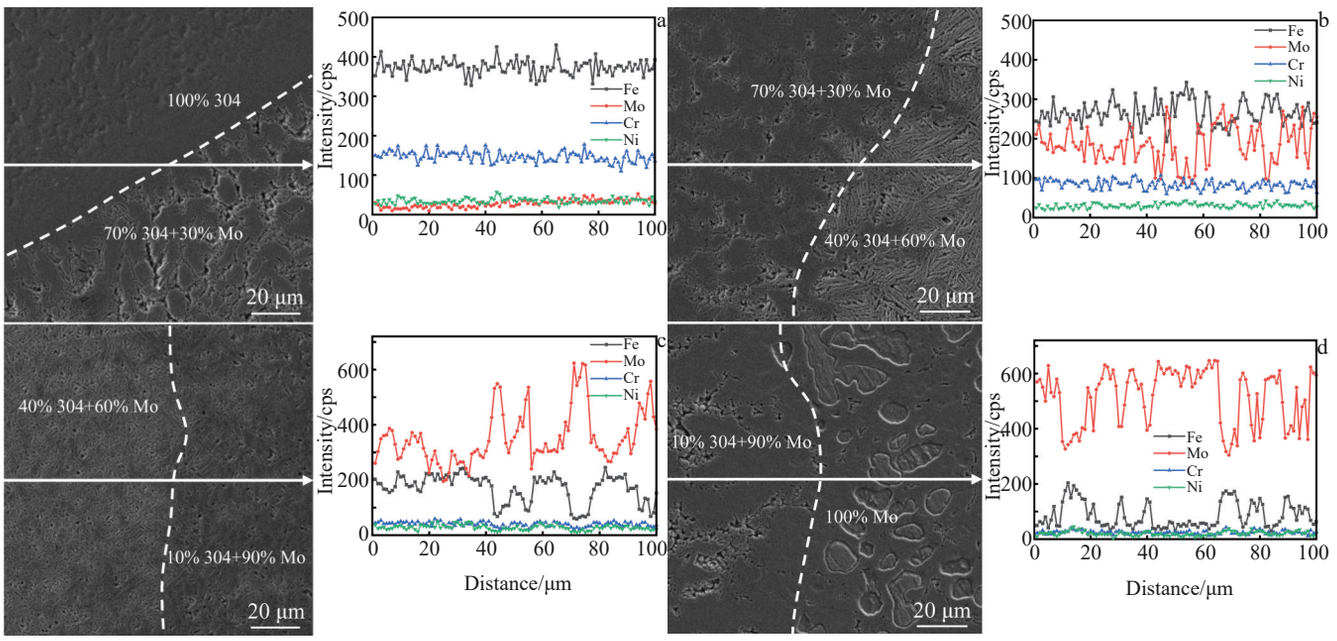

Fig. 10 SEM images and EDS line scanning results of adjacent interfaces with different Mo cotnent on *y*-*z* plane of S3 sample: (a) 0%–30%; (b) 30%–60%; (c) 60%–90%; (d) 90%–100%

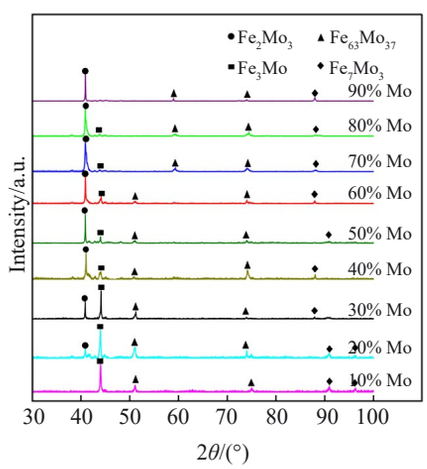

Fig. 11 XRD patterns of different positions of S2 sample

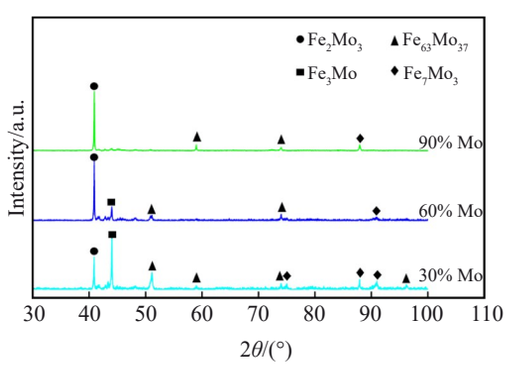

Fig. 12 XRD patterns at different positions of S3 sample

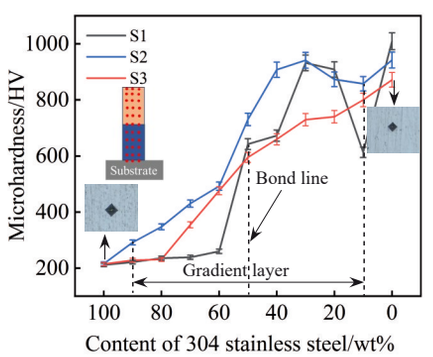

Fig. 13 Microhardness curves of three samples

and Fig. 14c that the trend of the COF curves of the sample is similar. Due to the cold welding effect between the grinding ball and the surface of the friction sample, after the initial stage of generating wear, the appearance of abrasive debris on the surface of the sample makes the roughness increase substantially, and the surface structure of the sample is gradually deteriorated, leading to the formation of more abrasive particles under the action of the grinding ball, which exhibits a higher COF[33]. With the prolongation of the friction time, the wear surface of the sample and the top of the counter-abrasive ball undergo shearing, abrasion, and other processes, and the COF tends to stabilize.

It can be seen from the previous analysis that the 304 stainless steel prepared by EB-DED has a high microhardness, so its COF is low, and the friction effect of the grinding ball on the friction surface is not obvious. With the increase in Mo content, the microstructure of the sample becomes denser, and the sample shows higher microhardness, a small COF, and significantly improved wear resistance. As shown in Fig. 14b, for Fe-Mo FGMs with a composition change rate of 10%, with the increase in Mo content, the material has high surface microhardness (Fig. 13) and dense structure (Fig. 5), and the wear resistance is improved more significantly. The average

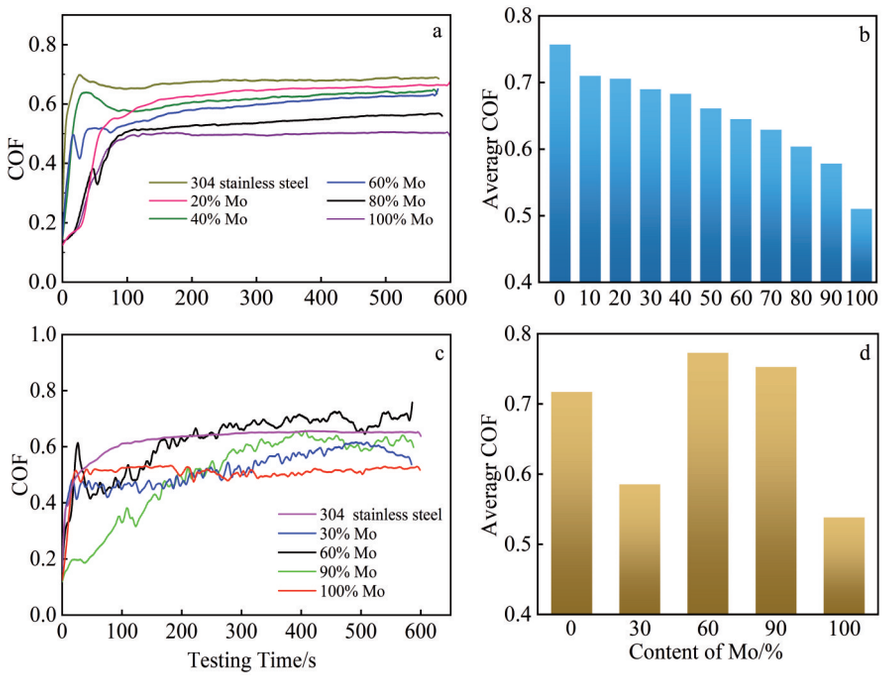

Fig.14 COF curves (a, c) and average COF (b, d) of S2 sample (a–b) and S3 sample (c–d)

COF along the composition gradient direction gradually decreases, indicating that the friction effect of the grinding ball on the surface of sample becomes less and less obvious, and the surface wear resistance gradually increases. In addition, the hard phase in the sample can be used as a carrier of load and shear force to significantly improve the wear resistance of the material[34]. For the Fe-Mo FGMs with a composition change rate of 30%, as shown in Fig. 14d, the hard phase content changes rapidly, the hardness distribution is uneven and the microhardness value is low, resulting in irregular fluctuations of the COF. The average COF of each deposition layer is quite different, so the wear resistance of the S3 sample is worse than that of S2, and the ability to resist deformation is insufficient.

Based on the abrasion profiles obtained by the 3D profilometer along the deposition direction, it is evident that the abrasion depths in the 304 stainless steel regions of samples S2 and S3 are greater than those in the Mo region. This trend is visible in Fig. 15a–15b and Fig. 15e–15f. In the middle region of the samples, as depicted in Fig. 15c–15d, a similar wear mark cross-sectional shape is observed, falling between the 304 stainless steel and Mo regions in terms of magnitude. The top region of the S2 sample exhibits the narrowest and the shallowest wear profile, resulting in the smallest loss of wear volume, and indicates better friction wear performance. Comparatively, the S3 sample demonstrates similar but poorer friction wear performance.

According to Eq. (2), the specific wear rates in different areas of S2 and S3 samples were analyzed and calculated, as shown in Fig. 16. The specific wear rate is the most direct parameter reflecting the wear resistance of the sample surface[35]. The specific values for S2 sample from bottom to top are 1.75×10^{-13}, 0.85×10^{-13}, and 0.30×10^{-13} m^3/Nm, and are 1.69×10^{-13}, 1.51×10^{-13}, 0.50×10^{-13} m^3/Nm for S3 sample. The trend of wear resistance coincides with the previous analysis, with high microhardness, good abrasion resistance, and a small specific wear rate. The top region of the S2 sample with a compositional variation of 10% exhibits the lowest specific wear rate, indicating the best wear resistance. The S3 sample with a compositional variation rate of 30% has a high specific wear rate in the middle region, but its wear resistance is poor.

The SEM images of the wear mark surfaces are given in Fig. 17 and Fig. 18. The presence of abrasive and adhesive wear can be seen in the obtained SEM images, where the main areas of 304 stainless steel exhibit abrasive wear. The plow furrows parallel to the sliding direction of the sample and wear debris are present in the abrasion scars, as shown in Fig.17a and Fig.18a, which are usually caused by the removal of material due to the surface sliding of the hard particles concerning the surface of material[36]. The presence of deeper furrows and deep grooves on the surface significantly reduces the wear resistance of the samples. And the relatively deep furrows and grooves observed in the wear morphology of the S2 sample with a compositional change rate of 30% corroborate the poor wear resistance of the S3 sample. Mo region is not prone to friction under dry sliding conditions due to its high hardness and good thermal conductivity. The abrasion marks are very shallow (even invisible) and narrow, so the main wear region of Mo exhibits an adhesive wear mechanism with a small amount of abrasive wear, as shown in Fig.17j and Fig.18e, demonstrating its excellent wear resistance.

3.5 Effect of compositional change rate on compressive properties

Fig.19 compares the compressive stress-strain curves of the S2 and S3 samples. In all cases, compression testing was

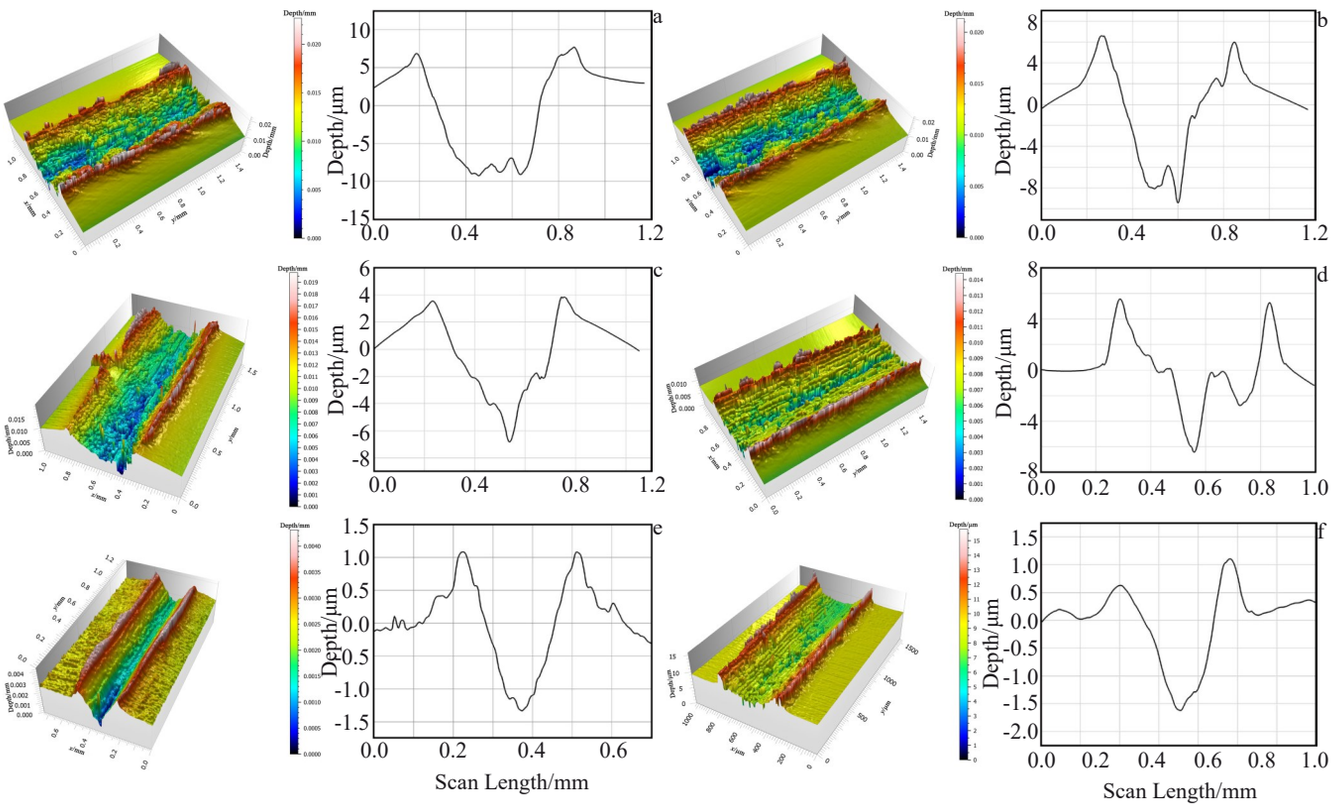

Fig.15 Optical 3D and 2D profiles obtained for different regions of S2 sample (a, c, e) and S3 sample (b, d, f): (a–b) bottom; (c–d) middle; (e–f) top

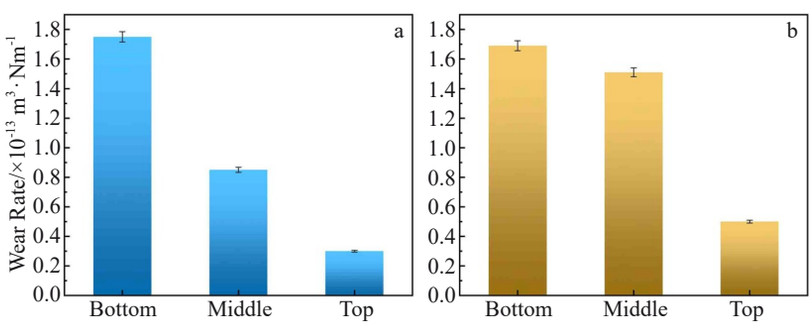

Fig.16 Specific wear rate of S2 sample (a) and S3 sample (b)

carried out until the samples fractured. The compressive strength of the S2 and S3 samples increases gradually with the increase in Mo content. The fracture stress of the S2 sample increases from 595.10±11 MPa at the bottom to 750.05±14 MPa at the top, and the corresponding fracture strain increases from 12.56%±3% to 17.68%±6%. The fracture stress of the S3 sample increases from 465.74±10 MPa at the bottom to 526.66±7 MPa, and the corresponding fracture strain increased from 9.02%±2% to 9.41%±4%. Considering the fracture stress and the corresponding fracture strain, it can be concluded that the compression performance of the S2 sample is better than that of the S3 sample.

Fig. 20 shows the surface morphologies of compression fracture of S2 and S3 samples, and the damage of compression samples occurred in the middle position. The fracture of S2 and S3 samples is smooth, and very obvious cleavage steps and river patterns can be seen, which indicates that brittle fracture occurs in the vertical compression sample during the compression test, and the fracture type is cleavage fracture. The fracture surfaces of the S2 sample with 10% compositional change and the S3 sample with 30% compositional change both have a certain number of cracks, but the crack content of the S3 sample is higher than that of the S2 sample. The compression morphologies of the top region, as shown in Fig.20c and 20f, the fracture of the interface region of the S3 sample is relatively flat, and the fracture mode is manifested as a deconvoluted fracture, presenting a river-like pattern. And obvious microcracks can be seen on the fracture surface, which is characterized by obvious brittle fracture characteristics. The fracture morphology of the S2 sample is also characterized by brittle fracture characteristics, but more tear ribs are present on the fracture surface, as shown in

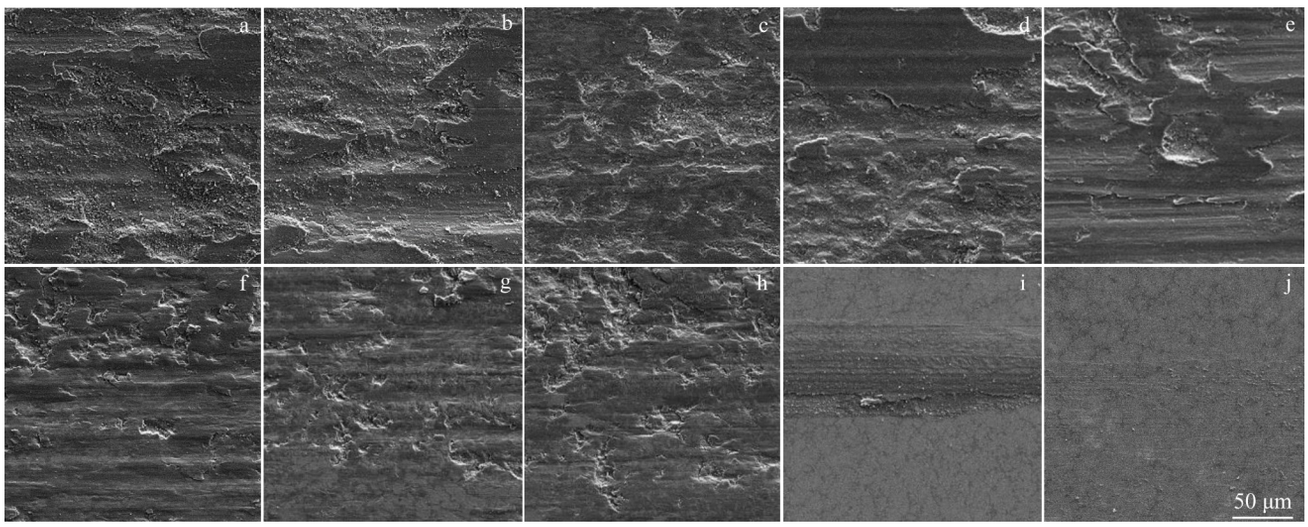

Fig.17 SEM images of wear surfaces of S2 sample with different Mo content: (a) 10%; (b) 20%; (c) 30%; (d) 40%; (e) 50%; (f) 60%; (g) 70%; (h) 80%; (i) 90%; (j) 100%

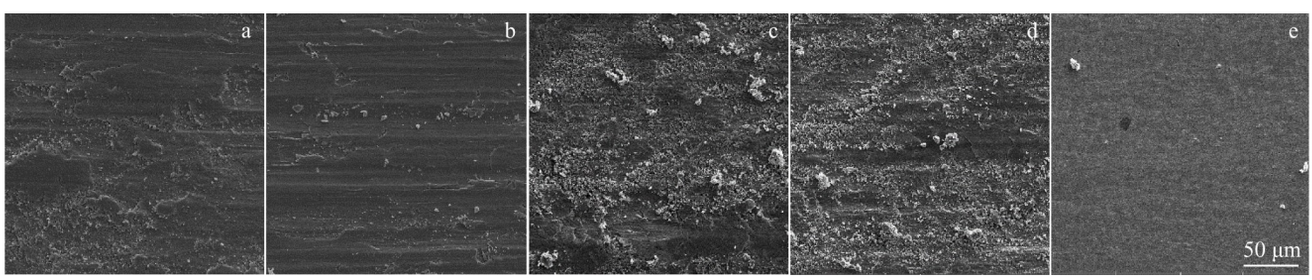

Fig.18 SEM images of wear surfaces of S3 sample with different Mo content: (a) 0%; (b) 30%; (c) 60%; (d) 90%; (e) 100%

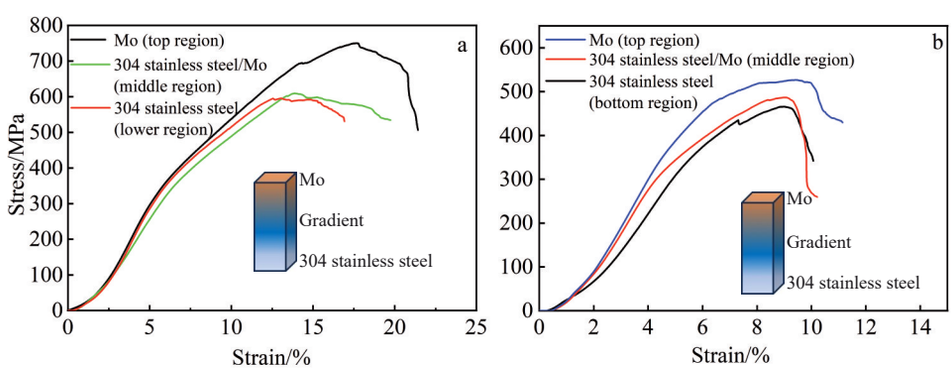

Fig.19 Engineering stress-engineering strain curves at different locations of S2 sample (a) and S3 sample (b)

Fig. 20c, which implies that the brittleness of the interfacial region is improved, and the compression performance of S2 sample is better than that of S3 sample.

4 Discussion

4.1 Microstructure evolution during EB-DED process and formation of Fe-Mo phase

The solidification pattern in AM processes is determined by the ratio (G/R) of the temperature gradient (G) to the growth rate (R). In this process, lower G/R ratios result in the formation of dendritic structures in the deposited layer, especially in the presence of elements (e.g. Mo) whose solidification equilibrium partition coefficients are significantly less than 1. As the Mo content and the height of the deposited layer increase, the temperature gradient and cooling rate gradually decrease. The microstructural morphology of Fe-Mo FGMs varies in different parts, mainly including columnar crystals, cytosolic crystals, and dendritic crystals.

As demonstrated by Reichardt et al[29], columnar grains were the result of partial remelting of the previously deposited layer, which allowed the previous grains to act as nucleation sites for the solidification of subsequent layers. During the

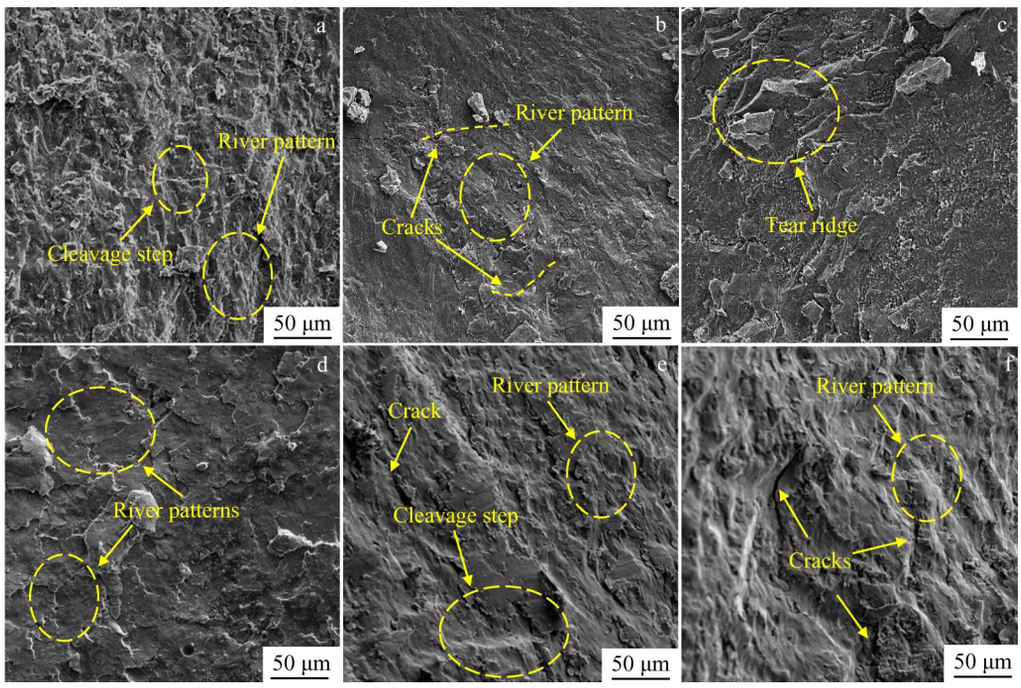

Fig.20 Fracture morphologies of S2 sample (a–c) and S3 sample (d–e) at different locations: (a, d) 304; (b, e) 304/Mo; (c, f) Mo

deposition process, the subsequently deposited layer remelted the organized regions on the surface of the previously deposited layer. The chemical composition and growth direction of the grains in the molten pool were close to those of the grains underneath the remelted zone, which provided conditions for continuous grain growth[37]. With the increase in Mo content, the number of alloying elements in the liquid-phase molten pool increased, and the solute concentration rose, leading to compositional supercooling, an increased nucleation rate, and the formation of finer dendrites during solidification[38].

The key reasons for the formation of the Fe-Mo phase in the EB-DED process are the homogenization and mixing of the elements Fe and Mo in the molten pool, and the achievement of the designed near-equivalent atomic composition. The EB-DED process used in this experiment has three special features, which help to promote the mixing and homogenization of elements Fe and Mo, thus contributing to the formation of the Fe-Mo phase, as shown in Fig. 21. Firstly, a stable eutectic pool is formed by precisely controlling the feeding and melting of Fe and Mo wires to achieve a continuous droplet transition. In this dual-feeder simultaneous feeding mode, the Fe and Mo wires have already melted into droplets and started mixing before entering the molten pool, which allows the elements to fully diffuse and undergo metallurgical reactions in the droplets while avoiding metal splashing. The results show that, firstly, the overall chemical composition of the melt pool (Fe/Mo ratio) is essentially consistent with the design values, although a small amount of Fe may be lost through evaporation. Secondly, when a droplet enters the molten pool, the elements Fe and Mo have enough time to further diffuse and to mix in the molten pool due to the high heat input in the EB-DED process, the stirring effect of the electron beam, and the low cooling rate in the vacuum environment. Thirdly, during the multilayer deposition process of EB-DED, the previous layer or even the first few layers may remelt when a new layer is deposited, which is manifested as a continuous microstructure in the Fe-Mo FGMs parts (as shown in Fig. 5 – Fig. 6). In addition, the remelting of elemental bias zones further promotes the homogenization of elemental distribution.

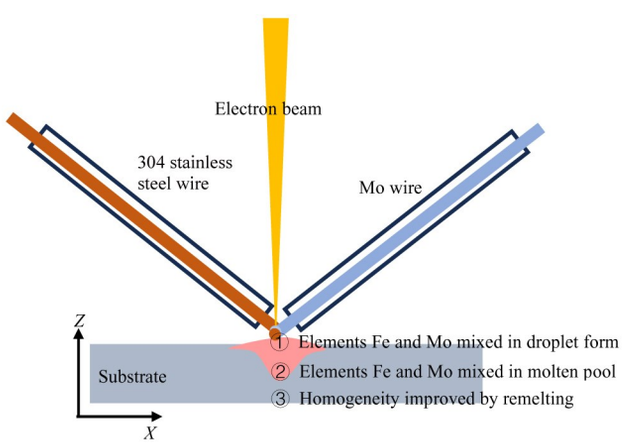

Fig.21 Mixing process of elements Fe and Mo during EB-DED

4.2 Strengthening mechanisms for hardness, wear resistance and compression properties

The enhancement of hardness in metallic materials can be achieved through various strengthening mechanisms, including solid solution strengthening and precipitation strengthening, which have the greatest influence in the gradient direction. As the Mo content increases, Mo gradually

dissolves into the Fe solid solution, distorting the solid solution lattice. The accumulated Mo in the previously deposited layer eventually precipitates in the form of intermetallic compound phases, leading to the gradual increase in the hard phase Fe_2Mo_3 in the Fe-Mo FGMs. This phenomenon significantly enhances the microhardness of the material through solid solution strengthening and precipitation strengthening[39–40].

The wear resistance of materials is closely linked to their hardness and strength. In the gradient interface area of the deposited layer, the combination of adhesive and abrasive wear mechanisms depends on the composition of sample. The presence of the strengthening phase in the deposited layer significantly enhances hardness and strength. Refinement of grains increases the number of grain boundaries, effectively impeding plastic deformation caused by the load in wear experiments. This weakens adhesion and the bearing capacity of the GCr15 steel ball to the material, promoting the transfer of load from the soft matrix to the hard particles. This effect can effectively shield the matrix from further fragmentation, and prevent the sample surface from easily peeling or falling off due to friction and wear, resulting in excellent friction performance[41].

During the compression process of Fe-Mo FGMs, due to the large difference in the thermal expansion coefficients of 304 stainless steel and Mo, when the composition change rate is high, the huge thermal stress inside the sample leads to different deformation of different materials, resulting in micro-cracks inside the sample[42]. In the compression process, it becomes a fracture source and reduces the overall compressive strength of the sample. However, from the analysis of the microstructure in Fig. 5–Fig. 6, it can be seen that there are no obvious defects such as cracks in the Fe-Mo FGMs prepared by directional energy deposition AM. The cracks on the surface in Fig. 20 are under the action of huge pressure. The internal microcrack source gradually expands and eventually forms a large crack. In the gradient transition region, however, good interfacial metallurgical bonding not only enhances the overall strength of the material but also effectively prevents the expansion of cracks and enhances the anti-cracking properties of the material, so that the material can maintain excellent mechanical properties under complex stress conditions.

5 Conclusions

1) The Fe-Mo direct joining materials prepared by the EB-DED technique show unfused Mo droplets and cracks at the interface, which resulted in poor interfacial bonding properties and susceptibility to failure. The Fe-Mo FGMs with compositional variations of 10% and 30% have a dense microstructure that varies continuously along the direction of the deposition height (*z*-direction). With the increase in Mo content, the strong metallurgical bonding between the deposited layers is formed.

2) The EDS results show that the Fe-Mo FGMs with a compositional change rate of 10% have a smoother compositional transition with the increase in the number of gradient layers, a uniform transition of the major elemental contents of Fe and Mo, and a full diffusion between the layers without any abrupt changes. The higher rate of compositional change leads to faster changes in microstructure and elemental content, and cracks appear at the interface, resulting in the decrease in bond strength.

3) The results of microhardness tests show that the microhardness is positively correlated with the Mo content. The microhardness of the sample increases gradually along the height direction, and the microhardness of the FGMs with a compositional change rate of 10% is up to 940 HV. The average COF decreases gradually, which improves the wear resistance of the material and reduces the wear rate. And the top region shows excellent resistance to surface wear.

4) The compressive failure mechanism of Fe-Mo FGMs with different compositional change rates is mainly characterized by brittle fracture. And when the compositional gradient changes too rapidly, the mismatch of the thermal expansion coefficients of the deposited materials leads to severe thermal cracking, which significantly reduces the compressive properties of the materials. The samples with a compositional change of 10% have better compressive properties, with a compressive fracture stress of 750.05±14 MPa in the top region, which is 42% higher than that of the FGMs with a compositional change of 30%.

References

1 Loh G H, Pei E, Harrison D *et al*. *Additive Manufacturing*[J], 2018, 23: 34

2 Ghanavati R, Naffakh-Moosavy H. *Journal of Materials Research and Technology*[J], 2021, 13: 1628

3 Derazkola H A, Garcia E, Murillo-Marrodán A. *Journal of Materials Research and Technology*[J], 2023, 25: 7254

4 Aghajani Derazkola H, Garcia E, Murillo-Marrodán A. *Journal of Materials Research and Technology*[J], 2022, 19: 3172

5 Zhang Bangyan, Wu Hongbin, Dong Jiajian *et al*. *Failure Analysis and Prevention*[J], 2023, 18(2): 71 (in Chinese)

6 Zhou Hongdeng, Xu Wenjin, Tian Qingchao. *Steel Tube*[J], 2023, 52(1): 78 (in Chinese)

7 Li Xinglong, Tan Xue, Lv Jianyang *et al*. *Chinese Patent*, CN110952090B[P], 2021

8 Wang W R, Hua M, Wei X C. *Wear*[J], 2011, 271(7): 1166

9 Wang H T, Wang G Z, Xuan F Z *et al*. *Engineering Failure Analysis*[J], 2013, 28: 134

10 Tian X X, Zhao Z, Wang H B *et al*. *Journal of Alloys and Compounds*[J], 2023, 960: 170687

11 Li T X, Wang Z J, Yang Z W *et al*. *Journal of Alloys and Compounds*[J], 2022, 915: 165398

12 Kim S H, Lee H, Yeon S M *et al*. *Additive Manufacturing*[J], 2021, 47: 102288

13 Fathi R, Wei H, Saleh B *et al*. *Applied Materials Today*[J], 2022, 26: 101373

14 Pradeep A D, Rameshkumar T. *Materials Today: Proceedings*[J], 2021, 45: 729

15 Rajasekhar K, Suresh Babu V, Davidson M J. *Materials Today: Proceedings*[J], 2021, 41: 1156

16 Tammas-Williams S, Todd I. *Scripta Materialia*[J], 2017, 135: 105

17 Osipovich K S, Astafurova E G, Chumaevskii A V *et al*. *Journal of Materials Science*[J], 2020, 55(4): 1

18 Shu X, Chen G Q, Liu J P *et al*. *Materials Letters*[J], 2018, 213: 374

19 Chen X Y, Han J, Wang J *et al*. *Materials Letters*[J], 2021, 300: 130141

20 Zuback J S, Palmer T A, DebRoy T. *Journal of Alloys and Compounds*[J], 2019, 770: 995

21 Shah K, Haq I, Khan A *et al*. *Materials & Design*[J], 2014, 54: 531

22 Yao M X, Yao Z J, Tao X W *et al*. *Vacuum*[J], 2024, 227: 113343

23 Xin D Q, Yao X C, Zhang J *et al*. *Journal of Materials Research and Technology*[J], 2023, 23: 4135

24 Qiu Z K, Zhang P Z, Wei D B *et al*. *Tribology International*[J], 2015, 92: 512

25 Bobbio L D, Otis R A, Borgonia J P *et al*. *Acta Materialia*[J], 2017, 127: 133

26 Reisgen U, Sharma R, Oster L. *Metals-Open Access Metallurgy Journal*[J], 2019, 9(7): 745

27 Nagasai B P, Malarvizhi S, Balasubramanian V. *Journal of Materials Processing Technology*[J], 2022, 307: 117655

28 Chaurasia J K, Jinoop A N, Parthasarathy P *et al*. *Optik*[J], 2021, 246: 167766

29 Reichardt A, Dillon R P, Borgonia J P *et al*. *Materials & Design*[J], 2016, 104: 404

30 Emadinia O, Zafar F, Fiorentin F *et al*. *Procedia Structural Integrity*[J], 2024, 53: 278

31 Li S L, Li S F, Liu L *et al*. *International Journal of Plasticity*[J], 2024, 176: 103951

32 Li S D, Liu D F, Liu G *et al*. *Surface and Coatings Technology*[J], 2023, 475: 130155

33 Feng C N, Zhang D K, Chen K *et al*. *International Journal of Mechanical Sciences*[J], 2018, 142–143: 140

34 Huang S W, Samandi M, Brandt M. *Wear*[J], 2004, 256(11): 1095

35 Tao X W, Yao Z J, Zhang S S. *Materials Letters*[J], 2018, 225: 13

36 Shu C Q, Yao Z J, Du W B *et al*. *Vacuum*[J], 2022, 206: 111513

37 Dinda G P, Dasgupta A K, Mazumder J. *Materials Science and Engineering A*[J], 2009, 509(1): 98

38 Zhu Y Y, Li J, Tian X J *et al*. *Materials Science and Engineering A*[J], 2014, 607: 427

39 Wu D J, Song C C, Di T D *et al*. *Composites Part B: Engineering*[J], 2022, 235: 109736

40 Brandl E, Schoberth A, Leyens C. *Materials Science and Engineering A*[J], 2012, 532: 295

41 Mølgaard J. *Wear*[J], 1976, 40(3): 277

42 Liu S Y, Shin Y C. *Materials & Design*[J], 2017, 136: 185

电子束定向能量沉积Fe-Mo功能梯度材料的微观组织及性能

李丹妮[1,2]，姚正军[1,2]，姚孟欣[1]，张叔贤[1]，Moliar Oleksandr[3]，Soloviova Tetiana[3]，Trosnikova Iryna[3]，Loboda Petro[3]，张莎莎[1]

(1. 南京航空航天大学 材料科学与技术学院，江苏 南京 211100)

(2. 面向苛刻环境的材料制备与防护技术工业和信息化部重点实验室，江苏 南京 210016)

(3. 乌克兰国立技术大学 伊戈尔·西科尔斯基基辅理工学院，乌克兰 基辅 03056)

摘　要：利用电子束定向能量沉积（EB-DED）技术，制备了沿成分梯度方向从100% 304不锈钢到100% Mo的不同成分变化率的Fe-Mo功能梯度材料（FGMs），包括成分突变100%、成分变化率10%和成分变化率30% 3种试样。结果表明，成分变化率显著影响试样的显微组织和力学性能。在成分突变的试样中，304不锈钢和Mo之间成分急剧变化导致了两种材料界面附近的组织形态和硬度有很大的差异。而随梯度层数的增加，成分沿沉积高度方向连续变化，显微组织形貌呈现出从304不锈钢到Mo的平滑过渡，由柱状晶逐渐转变为树枝晶。Fe、Mo等主要元素沿梯度方向呈线性转变，沉积层间扩散充分，冶金结合良好。成分梯度变化越小，沿沉积方向的显微硬度值越大。当成分梯度为10%时，梯度层显示出更高的硬度（最高达940 HV）和优异的抗表面磨损性能，且试样整体压缩性能较好，顶部区域的压缩断裂应力达到750.05±14 MPa。

关键词：功能梯度材料；EB-DED；微观组织演变；力学性能

作者简介：李丹妮，女，1998年生，硕士生，南京航空航天大学材料科学与技术学院，江苏 南京 211100，E-mail：515124727@qq.com